ISSN 1063-7834, Physics of the Solid State, 2019, Vol. 61, No. 7, pp. 1203–1210. © Pleiades Publishing, Ltd., 2019.
Russian Text © The Author(s), 2019, published in Fizika Tverdogo Tela, 2019, Vol. 61, No. 7, pp. 1262–1269.

MAGNETISM

Tunnel Conductivity and Tunnel Magnetoresistance of the Fe–SiO Films: Interplay of the Magnetotransport and Magnetic Properties

D. A. Balaev[a, *] and A. D. Balaev[a]

[a] *Kirensky Institute of Physics, Krasnoyarsk Scientific Center, Siberian Branch, Russian Academy of Sciences, Krasnoyarsk, 660036 Russia*

**e-mail: dabalaev@iph.krasn.ru*

Received March 5, 2019; revised March 5, 2019; accepted March 5, 2019

Abstract—The electrical properties of a system of nanogranular amorphous Fe–SiO films with a SiO concentration between 0 and 92 vol % have been investigated. The samples with a low SiO content are characterized by the metal-type conductivity. With an increase in the dielectric content x in the films, the concentration transition from the metal to tunneling conductivity occurs at $x \approx 0.6$. At the same concentration, the ferromagnet–superparamagnet transition is observed, which was previously investigated by the magnetic method. The temperature dependences of the electrical resistivity $\rho(T)$ for the compositions corresponding to the dielectric region obey the law $\rho(T) \sim \exp(2(C/kT)^{1/2})$, which is typical of the tunneling conductivity. The estimation of the metal grain sizes from the tunneling activation energy C has shown good agreement with the sizes obtained previously by analyzing the magnetic properties. In the dielectric region of the compositions, the giant magnetoresistive effect attaining 25% at low temperatures has been obtained.

DOI: 10.1134/S1063783419070047

1. INTRODUCTION

At present, there still has been a keen interest in the magnetic, transport, and magnetotransport properties of heterogeneous systems consisting of ferromagnetic metal nanoparticles in a dielectric matrix [1–25]. This is due to the giant magnetoresistance [2–6, 8, 10, 12, 16–19, 21–25] and anomalous Hall effect [13, 19, 21] in the transport properties, which, together with the magnetic behavior determined by a small size of magnetic particles, attach particular importance to the study of the magnetotransport properties of ferromagnetic metal–dielectric systems.

It is worth noting that the study of the magnetic and electrical properties of granular crystalline 3-*d* metal–dielectric films began long time ago [26, 27]. It was found that, with an increase in the dielectric concentration (SiO_2 or Al_2O_3 in cermets with Ni [26] and Co [27]), these systems undergo a ferromagnet–superparamagnet concentration transition; in this case, the characteristic electrical conductivity changes from metal-type to tunneling. To date, there has been a great number of studies on the magnetic and transport properties of such two-phase systems in the form of thin films with different ferromagnetic metals (M) and dielectrics (D) [1–5, 9, 11–13, 17–28]. In the dielectric concentrations region x ($M_{1-x}D_x$), the tunneling conductivity is implemented and the temperature dependence of the resistivity $\rho(T)$ has a typical form $\ln(\rho(T)) \sim T^{-0.5}$ [1, 6, 12, 15, 17–20, 22–28]. In this case, the $M_{1-x}D_x$ systems in the concentration range corresponding to the tunneling conductivity can exhibit the giant magnetoresistance effect [17–19, 22–27, 29]. This spin-dependent tunneling is related to the fact that when an electron tunnels from one grain to another, the resistivity will depend on the direction of magnetizations μ in these grains. The resistance of a tunnel contact at $\mu_1 \uparrow\downarrow \mu_2$ will be higher than at $\mu_1 \uparrow\uparrow \mu_2$ [27, 29].

In this work, we report the results of investigations of the temperature dependences of electrical resistivity and magnetoresistance $\rho(H)$ for the Fe–SiO films. The Fe–SiO composite system holds an intermediate position between crystalline granular metals and amorphous alloys. In this system, the amorphous state of a metal in a grain (cluster in a dielectric matrix) is implemented. The study is organized as follows. In Section 2, we briefly overview the magnetic properties of the Fe–SiO film system studied previously in [30–32] and present a phase diagram of the magnetic state, which is required to interpret the electrical resistivity and magnetoresistance data. Section 3 includes the results of investigations of the $\rho(T)$ dependences for the Fe–SiO films and their analysis for the dielectric concentration region using the tunneling conductivity mechanism [27–29]. Section 4 presents the data on

Table 1. Parameters of the investigated Fe–SiO films. The first column shows the SiO content during deposition; x is the dielectric content (SiO_y) obtained after correction of the compositions (see Section 2); β is the exponent determined from the condition $\ln(\ln\rho) \sim \beta\ln T$, $\langle d\rangle$, d_{min}, and d_{max} are the average, minimum, and maximum iron grain sizes obtained from the magnetic data [32, 40]; and d(4 K), d(78 K), and d(300 K) are the grain sizes determined using Eqs. (3) and (6) (see Section 3)

vol % SiO	x	β	$\langle d\rangle$, nm	d_{min}–d_{max}, nm	d(4 K), nm	d(78 K), nm	d(300 K), nm
65	0.59	–	–	–	–	–	–
69	0.615	0.4	–	–	–	–	–
72	0.645	0.42	3	1–8	4.5	1.1	0.5
75	0.675	0.52	3	1–8	5.5	1.3	0.6
77	0.69	0.54	2.8	1–8	5.5	1.3	0.6
88	0.78	0.5	1.6	0.5–5.5	5.6	1.3	0.7
92	0.83	0.5	1.3	0.5–4.5	4.6	1.1	0.5

the magnetoresistive effect, which is also adequately described in the framework of the tunneling magnetoresistance mechanism. In Section 5, conclusions are drawn.

2. MAGNETIC PHASE DIAGRAM OF THE Fe–SiO FILMS

The Fe–SiO films were formed by vacuum evaporation; the SiO volume concentration ranged from 0 to 92 vol %. Films with a Fe thickness of ~100 nm on a Pyrex substrate were used. The electron microscopy data showed [30, 31] that the films with a SiO content below 17 vol % are microcrystalline and have a crystallite size of ~30–40 nm; in the SiO concentration range of ~17–35 vol %, the film structure is a mixture of the crystalline and amorphous phases with a cluster (grain) size of 25–30 nm; finally, at high concentrations, the samples are completely amorphous.

The measurements of the magnetic properties of the film with SiO concentrations above 69 vol % showed that the magnetic moment μ_{at} per iron atom starts sharply decreasing at a SiO content above 70 vol % [32] (see Section 3). It is reasonable to attribute this behavior to the fact that, with an increase in the SiO concentration, some silicon atoms leave the unstable SiO compound ($SiO \rightarrow 1/2Si + 1/2SiO_2$) [33] with the formation of a chemical bond with iron. At the same time, the grain composition gradually changes from pure iron to the compositions similar to Fe_3Si, Fe_5Si_3, ... and FeSi. Additional measurements of the temperature dependence of the magnetic susceptibility revealed a peak near ~350 K, which is close to the Néel temperature of the bulk FeSi compound (450 K [34]), taking into account that the temperature of magnetic ordering of the nanosized complexes decreases [35, 36]. This indirectly confirms the formation of iron and silicon compounds on the grain surface in the system under study. This circumstance, which is noncritical for interpreting the magnetic properties [30–32], requires correction of the dielectric concentration when explaining the electrical properties, since the Fe_3Si and FeSi compounds remain metals [34, 37, 38] and the real dielectric concentration (in this case, SiO_y, $1 \le y \le 2$) decreases. The film compositions were corrected assuming that each Si atom, when chemically bonding with a Fe atom, reduces its magnetic moment to zero [34, 39] and SiO_y acts as a dielectric. Hereinafter, the dielectric concentration x is the volume SiO_y content (from 0 to 0.83). The SiO contents used when forming the films (the first column) and the real dielectric content (the second column) are given in Table 1.

Figure 1 shows the magnetic phase diagram dielectric concentration x—investigated film system temperature. The dashed line shows the ferromagnet–paramagnet (FM–P) interface. This, in fact, is the Curie temperature Θ of grains, which decreases with increasing SiO content at the iron amorphization.[1] This interface at concentrations of up to $x = 0.59$ was determined by the spin-wave resonance (from the spin wave stiffness D) [30] and vibrating sample magnetometry (from the comparison of the temperature dependences of saturation magnetization with the Bloch's law) [31].

For the films with the higher x values, the phase diagram data (Fig. 1) were obtained by describing the experimental magnetization curves $M(H)$ [32, 40]. The description was based on the $M(H)$ dependences simulated at 4.2–300 K by the Langevin function, which describes the superparamagnetic (SP) behavior of the particle magnetic moment μ with regard to the particle size distribution. In addition, the $\mu(T)$ behavior (in the form of the Brillouin function) was taken into account, which allowed us to determine the Curie temperature Θ of the film and the SP–P interface. The interparticle interactions were taken into account by introducing the effective field $H_{eff} = H + \gamma M$, where the interaction constant γ is proportional to the inter-

[1] A factor stabilizing the amorphous state of grains in the films is silicon.

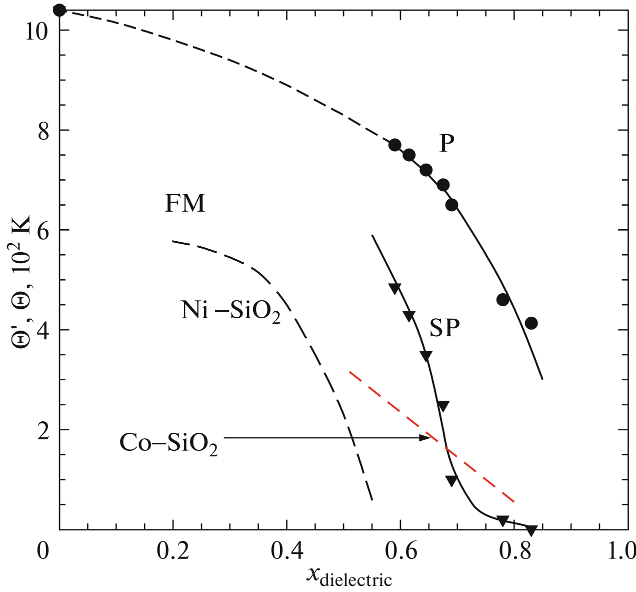

Fig. 1. Phase diagram of the Fe–SiO film system. x is the SiO_y dielectric concentration, Θ is the Curie temperature of iron grains, and Θ' is the intergrain ordering temperature. Regions with the ferromagnetic (FM), superparamagnetic (SP), and paramagnetic (P) states are shown. Dashed lines show the FM–SP interfaces for $Ni–SiO_2$ [26] and $Co–SiO_2$ [27] systems.

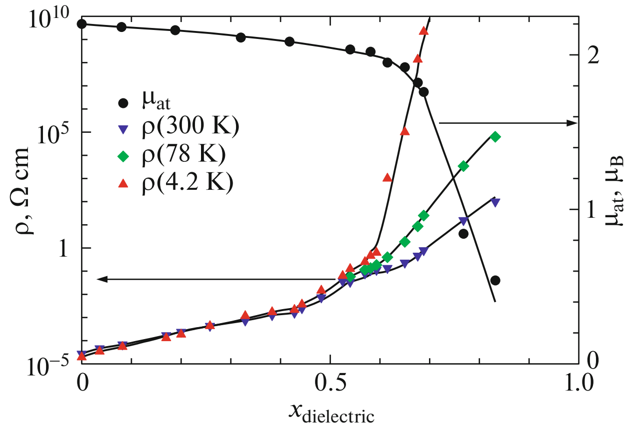

Fig. 2. Dielectric concentration dependence of the resistivity $\rho(x)$ (ρ, the left-hand scale) and iron atom magnetic moment μ_{at} (right-hand scale) at different temperatures.

grain ordering temperature Θ'. The described analysis makes it possible to distinguish the SP state of the films in the magnetic phase diagram (Fig. 1). For comparison, the FM–SP interfaces for the $Ni–SiO_2$ [26] and $Co–SiO_2$ [27] systems are shown.

It should be noted that the average iron grain size $\langle d\rangle$ in the SP concentration range is several nanometers. Table 1 gives the minimum (d_{min}) and maximum (d_{max}) particle sizes from the size distribution according to the condition $\int_{d_{min}}^{d_{max}} f(d)\partial(d) \approx 0.95$, as well as the average iron particle size $\langle d\rangle$ obtained by processing of the $M(H)$ dependences [32]. The magnetically inactive particle surface (the Fe–Si compound with a thickness of 1–2 atomic layers) is not included in the sizes d_{min}, d_{max}, and $\langle d\rangle$ [40].

3. TEMPERATURE DEPENDENCES OF THE ELECTRICAL RESISTIVITY OF THE Fe–SiO FILMS

The transport and magnetotransport properties were measured using a special insert in an automated vibrating sample magnetometer [41] by a standard four-probe method. Contacts were formed from an indium–gallium–mercury amalgam. For the compositions with the metal-type conductivity, a dc current mode was used and, for the compositions with the tunneling conductivity, a dc voltage mode. At the currents and voltages used (up to ~500 V for the dielectric composition region), the Ohm's law was valid. The distance between potential contacts was ~1 cm. An external field was applied parallel to the current direction in the film plane.

Figure 2 presents concentration dependences $\rho(x)$ at $T = 300$, 78, and 4.2 K. It can be seen that the film composition region can be divided into three portions: $0 < x < 0.45$ and $0.6 \le x \le 0.83$ with the metal and dielectric conductivities, respectively, and $0.45 \le x \le 0.6$ corresponding to the transition mode.

First, let us consider the metal-type conductivity mode. The $\rho(x = 0)$ is ≈5ρ of the value for bulk iron. As the dielectric content increases, the resistivity grows, the $\rho(T)$ behavior changes and, starting with $x \ge 0.35$, it becomes typical of the nonmetal conductivity. The temperature coefficient of the resistivity $\alpha = (1/\rho)\partial\rho/\partial T$ gradually decreases with increasing x and changes its sign. At $x = 0.3$, in the range of 100 K $\le T \le$ 300 K, the α value is only $\sim 2 \times 10^{-5}$ K^{-1} and, in principle, one can choose a composition with even smaller α. In addition, note that for samples in the range of $0.1 \le x \le 0.2$ near $T \sim 30$ K, there are the resistivity minima characteristic of nonequilibrium alloys. As the x value increases, the minimum temperature grows.

The $\rho(T)$ dependences for metal alloys are expressed by the phenomenological equation

$$\rho(T) = \rho_0 - a\log T + bT^2 + cT.$$

The $\rho(T)$ plots built with the use of this equation for concentrations between $0.1 \le x \le 0.2$ from the experimental data revealed the presence of all the four terms. The term proportional to $-\log T$ contributes to the region below the temperature of the $\rho(T)$ minimum; in the temperature range up to 100 K, the quadratic term T^2 dominates; after that, until room tem-

perature, the $\rho(T)$ dependence is proportional to T. The logarithmic term is apparently related to the s–d Kondo scattering. The quadratic term is related to scattering of s electrons by localized d electrons or to the spin density fluctuation. The linear term corresponds to the electron–phonon interaction.

The further growth of the dielectric content (Fig. 2) causes an increase in the film resistivity and, at a concentration of $x \approx 0.6$, the resistivity abruptly increases, which is especially pronounced at $T = 4.2$ K. This is caused by the collapse of an infinite metal cluster into individual particles. The transition mode changes for the dielectric one. The Fe or Fe_3Si grains are separated from each other by a SiO_y ($1 \leq y \leq 2$) dielectric spacer. The magnetic moment μ_{at} also shown in Fig. 2 starts sharply decreasing at the same value of $x \approx 0.6$. This decrease (see Section 2) is related to the formation of the FeSi antiferromagnetic compound on the grain surface. The infinite ferromagnetic cluster splits into ferromagnetic grains. The interrelation between the electrical and magnetic properties can be followed from the data in Fig. 2

In the dielectric composition range of $x = 0.6$–0.83 with an increase in temperature, and, correspondingly, in the SP region with a decrease in temperature, the $\rho(T)$ dependences steeply rise. Using the condition $\ln(\ln\rho) \sim \beta\ln T$, we determined the experimental β values (the exponent in the expression $\rho(T) \sim \rho_0\exp(T^{-\beta})$), which appeared to be about 0.5 (Table 1). As was mentioned in Introduction, the temperature dependence of the resistivity $\rho(T) \sim \exp(T^{-0.5})$ was frequently observed in granular systems [1, 6, 12, 15, 17–20, 22–28]. Without focusing upon advantages and drawbacks of different models [19–21, 26–29, 42] that yield the dependence $\ln(\rho(T)) \sim T^{-0.5}$, we interpret the experiment using the model proposed in [27–29].

In the dielectric mode, metal grains with size d are separated by spacings s. The conductivity is implemented via recharging of neighboring grains; electrons tunnel through the intergrain spacings s due to thermal activation. In the weak electric field mode ($e\Delta V \ll kT$,[2] where ΔV is the potential difference between neighboring grains, k is the Boltzmann constant, and e is the elementary charge), the conductivity σ is determined by the Boltzmann equation, in which the exponent includes, along with the tunneling probability $2\kappa s$ (κ is the reciprocal electron wavelength characterizing the electron wave function decay length in a dielectric [19, 27–29]), the term related to the charge energy E_C ($E_C \sim e^2/d$):

$$\sigma \sim \exp(-E_C/2kT - 2\kappa s). \quad (1)$$

Under the sufficiently strong simplification s/d = const for a specific film, the conductivity, as the function (s/d) at each temperature, has a maximum, and,

[2] According to our estimations based on the grain sizes, the conditions $e\Delta V \ll kT$ was met under the experimental conditions.

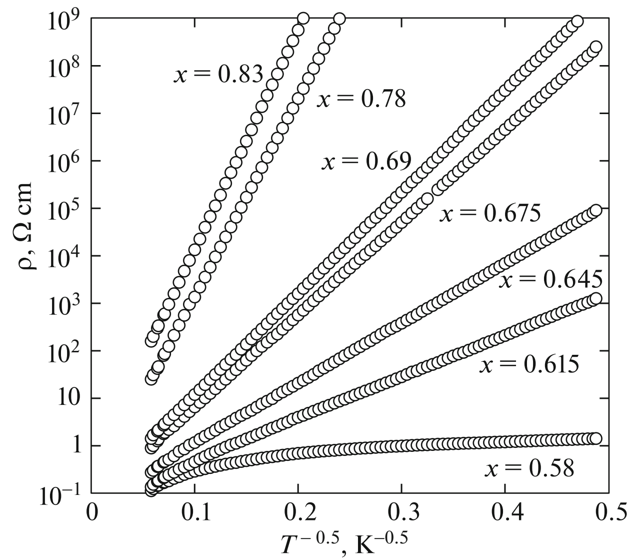

Fig. 3. Dependences of the electrical resistivity ρ on $T^{-0.5}$ for the samples with different volume dielectric concentrations x.

consequently, at each temperature there are the most probable intergrain spacings s_m through which the tunneling occurs. As a result, the $\rho(T)$ dependence has the form [27–29]

$$\rho(T) = \rho_0 \exp[2(C/kT)^{0.5}]. \quad (2)$$

In this equation, the tunneling activation energy C can be expressed through the probable intergrain spacings $s_m(T)$

$$s_m = (C/kT)^{0.5}/2\kappa. \quad (3)$$

Figure 3 shows the dependences of ρ (logarithmic scale) on $T^{-0.5}$ for the investigated films. It can be seen that, in the samples with $x = 0.615$–0.83, the experimental points fit fairly well straight lines, according to Eq. (2), and this dependence is valid in a wide temperature range of $4.2\text{ K} \leq T \leq 300$ K. With a decrease in the dielectric content ($x \leq 0.58$), one can observe the deviation from straight lines (Fig. 3), especially at high temperatures.

The inclination of the straights in Fig. 3 was used to determine the tunneling activation energies C (Eq. (2)) shown in Fig. 4 as a function of the dielectric concentration x. For such a concentration dependence one can obtain [27–29] the expression

$$C(x) = \eta \frac{\left[\left(\frac{\pi}{6(1-x)}\right)\right]^2}{\left(\frac{\pi}{6(1-x)}\right)^{1/3} - \frac{1}{2}}. \quad (4)$$

Equation (4) is valid at the x values not too close to unity and the parameter η, as applied to the experimental data on the metal–dielectric system, can be

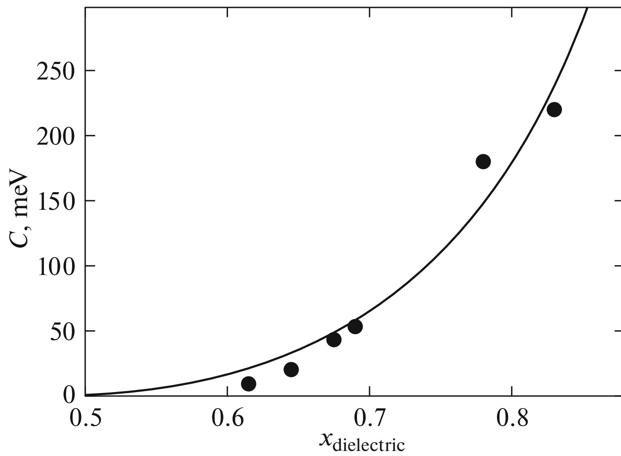

Fig. 4. Dielectric concentration dependence of the tunneling activation energy C. Dots show the experimental data and the solid curve, fitting using Eq. (4) at $\eta = 1.1$ eV.

considered to be fitting, although it has the meaning of a height of the tunneling barrier through which electrons tunnel. The data in Fig. 4 are satisfactorily described by Eq. (4) at $\eta = 1.1$ eV (solid curve in Fig. 4).

The parameter η is related to the characteristics of the dielectric spacers as

$$\eta = 2\kappa e^2/4\varepsilon_0\varepsilon, \qquad (5)$$

where ε_0 is the permittivity of vacuum and ε is the permittivity. The κ value is about 10^{10} m ($1/\kappa \sim 0.1$ nm) [19, 27–29]. Equation (5) corresponds to $\eta = 1.1$ eV, if we assume $\varepsilon \approx 15$. This is essentially higher than the value for bulk SiO_2 ($\varepsilon \approx 4$). In the investigated films, the dielectric spacers are formed by the amorphous silicon oxide SiO_y ($1 \le y \le 2$, see Section 2); most likely, there is the inhomogeneity in y in the space between metal grains. It is well known that the permittivity of SiO_y at intermediate y values increases several times as compared with the value for SiO_2 [43–45], which is quite consistent with the results of the analysis of the experimental $C(x)$ dependence using Eqs. (4) and (5). In addition, the tunneling barrier height U for silicon oxide SiO_y also significantly depends on y: for SiO_2, we have $U \approx 9$ eV, while for SiO, $U \sim 1$ eV [46, 47]. The tunneling barrier height determines the electron wave function decay length in the dielectric κ^{-1} according to the equation $\kappa^{-1} = (2meU/\hbar^2)^{-1/2}$ (m_e is the electron effective mass and $\hbar$ is the Planck's constant).

The η and U values have, in fact, the same meaning: $\eta \approx U$. At $U \approx 1.1$ eV, we have $\kappa^{-1} \approx 0.17$ nm [19, 27–29]. Therefore, the obtained value of $U \approx 1.1$ eV is quite consistent with the fact that the interlayer spacers between metal grains are formed by the SiO_y dielectric. Thus, the obtained concentration dependence $C(x)$ fits well the model representations used [27–29].

The spacings s and grain sizes d cannot be directly determined by comparing the experimental tunneling activation energies C, since s and d are included in them in the form of a ratio. According to Eq. (3), the dominant contribution to the electrical conductivity is made by different dielectric spacings at different temperatures. At high temperatures, the tunneling between small grains (high charge energies E_C) is caused by small spacings s. At low temperatures, the tunneling between large grains is preferred (low charge energies E_C and, consequently, large spacings s). It should be noted that this model is strongly simplified, since it does not take into account tunneling between grains of different sizes. However, since the measurement temperature range is wide, then, using Eq. (3), we can estimate the spacings s_m responsible for the charge transport at high and low temperatures from the experimental C values. After that, using the condition for determining the volume concentration x of a metal for a simple cubic lattice

$$s/d = \left(\frac{\pi}{6(1-x)}\right)^{1/3} - 1, \qquad (6)$$

we can recalculate the d values that will be maximum and minimum in the film, respectively. The d values given in Table 1 were obtained at temperatures of 4, 78, and 300 K. In the calculations, we used the κ^{-1} value obtained above (0.17 nm). The comparison of the minimum (d_{min}) and maximum (d_{max}) iron particle sizes from Table 1 that were obtained by processing of the magnetization curves [32] and the sizes d determined by analyzing the transport properties shows their good correlation. The d (300 K) and d (4 K) values hit the tails of the size distribution functions determined by the magnetic method, thereby confirming the average size $\langle d \rangle$ values.

4. TUNNEL MAGNETORESISTANCE

The samples in the dielectric concentration range exhibited the negative magnetoresistance. As an example, we present the data for the film with $x = 0.78$, which was characterized by the significant magnetoresistance $\Delta\rho/\rho_0 = [\rho(T) - \rho(H = 0)]/\rho(H = 0)$. According to the phase diagram (Fig. 2), there is a wide temperature range of the SP region for this sample. Figure 5 shows the dependences $\Delta\rho(H)/\rho_0$ for this film at temperatures of 31 and 180 K. It can be seen that the negative magnetoresistive effect $\Delta\rho/\rho_0$ at a temperature of 31 K attains 25% in a field of $H = 70$ kOe.

Since, as we showed in Section 3, in the concentration range of $x > 0.615$, the tunneling conductivity takes place; we interpret the results using the tunneling magnetoresistance mechanism [27, 29]. Mainly free

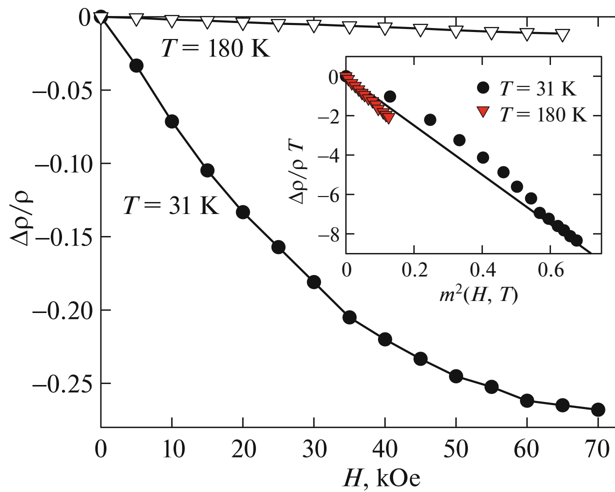

Fig. 5. Magnetoresistance $\Delta\rho(H)/\rho_0$ for the sample with a dielectric content of $x = 0.83$ at different temperatures. Inset: data in the coordinates $\Delta\rho/\rho_0 T$, $m^2(H, T)$; the line is built using Eq. (8) at $JP = 4$ meV.

electrons (s electrons) tunnel. During the tunneling event, the exchange coupling J_{sd} in grain 1 (donor) is broken, while in grain 2 (acceptor), it arises; i.e., the energy E_m of a tunneling electron in grain 2 and grain 1 occurs at the preserved spin in the tunneling process. The E_m value and sign depend on the mutual orientation of magnetic moments μ of neighboring grains and polarization P (polarization of s electrons by d electrons). When μ_1 and μ_2 are antiparallel, we have $E_m \geq 0$; when they are parallel, we have $E_m < 0$. The account for the additional term related to E_m in the exponent of Eq. (1) and the expansion of the right-hand side of Eq. (1) in the linear approximation in E_m terms (at $E_m/kT \leq 1$) leads to the formula [27, 29] describing the tunneling magnetoresistance

$$\begin{aligned}&[\rho(H) - \rho(H = 0)]/\rho(x = 0) = \Delta\rho/\rho_0 \\ &= -(JP/4kT)[m^2(HT) - m^2(h = 0, T)],\end{aligned} \tag{7}$$

where $m(H, T)^2 = (\mu_1\mu_2)/\mu^2$ is the squared relative magnetization.

According to Eq. (7), the magnetoresistance will be maximum at the FM–SP transition temperature [27, 29]. The temperatures at which the magnetoresistive effect was measured (Fig. 5) correspond to the SP phase and the temperature 31 K is close to the FM–SP interface (Fig. 1). It is this fact that apparently explains the giant magnetoresistive effect at 31 K.

In the SP state, $m^2(0, T) \equiv 0$ and Eq. (7) is rewritten in the form

$$\Delta\rho/\rho_0 = -(JP/4kT)m^2(H,T). \tag{8}$$

Therefore, the relative magnetoresistive effect should be described by the squared relative magnetization with the coefficient $JP/4kT$. The inset in Fig. 5 shows the magnetoresistance in coordinates $\Delta\rho/\rho_0 T$, $m^2(H, T)$; the magnetization data are taken from previous studies [32, 40]. It can be seen that the experimental data for a temperature of $T = 180$ K are described well by the linear dependence, according to (8), while at a temperature of 31 K, the agreement is much worse. Such a deviation from the predicted quadratic dependence was observed previously for different systems [8, 17, 18, 21, 24, 25] and attributed mainly to the effect of the distribution of ferromagnetic metal grains and, consequently, dielectric spacings. Indeed, in the conductivity and magnetoresistance calculation, the tunneling between the most probable intergrain spacings s_m determined from Eq. (3), through which tunneling occurs, is taken into account. According to the condition s/d = const (Section 3), it is necessary to take into account the contribution of the grains with sizes corresponding to the condition s/d = const to the magnetization, while the magnetization represents an integral characteristic of grains of all sizes. We estimated the value of JP using the data from Fig. 5 (inset) from the average inclination of the straights built by the least-squares method at the experimental points $\Delta\rho/\rho_0$ at two temperatures. According to Eq. (8), the value of JP was 4 meV (±20%). It is well known that the spin polarization P for s electrons in iron attains 0.44 [24, 48], which allows us to obtain $J \approx 9$ meV (±20%).

Previously [30], using the Bloch constant, the spin-wave stiffness constant D (100 meV Å^2) [30] was determined from the magnetic measurements for the film of the limit ferromagnetic composition $x = 0.615$ at which the Bloch law is still valid. The estimation of J by the expression $D = 2JS^2a^2$ (a is the lattice constant (≤3 Å) and $S = 1$) yields $J \approx 6$ meV. The exchange values determined by different methods were found to be in satisfactory agreement. It should be noted, however, that the Bloch's law allows one to experimentally determine the effective exchange, while the magnetoresistive effect, only the J_{sd} value. In addition, the comparison was made for different, though close, sample compositions. The estimation of J using the well-known mean-field theory expression $J = 3kT_C/2ZS(S + 1)$, where Z is the number of nearest neighbors, for the investigated film with $x = 0.78$ at $T_C = 452$ K (Fig. 1), $S = 1$, and $Z = 6$ yields $J = 4.9$ meV.

5. CONCLUSIONS

The study of the transport properties of the system of amorphous Fe–SiO nanocluster films and analysis of the results obtained together with the magnetic measurements data allowed us to draw the following conclusions. The role of a dielectric matrix in these films is played by the amorphous silicon oxide SiO_y ($1 \leq y \leq 2$) phase forming due to the partial formation of the Fe–Si compounds on the iron grain surface.

The concentration transition from the metal-type to tunneling conductivity was observed at a dielectric content of $x \approx 0.6$. This is caused by the collapse of an "infinite" metal cluster into individual nanoparticles. At the same dielectric concentration in the concentration– temperature phase diagram, the region corresponding to the superparamagnetic state of the magnetic moments of iron grains arises. In the dielectric composition region, the temperature dependence of the electrical resistivity is described by the expression $\rho(T) = \rho_0\exp[2(C/kT)^{0.5}]$, which is characteristic of the tunneling conductivity. The analysis of the concentration dependence of the tunneling activation energy C in the framework of the model used [27–29] showed satisfactory agreement with the characteristic parameters of the SiO_y dielectric and metal grain sizes determined previously from the magnetic measurement data. The film with a dielectric content of $x \approx 0.78$ exhibits the giant (for metal cermets) magnetoresistive effect $\Delta\rho(H)/\rho_0 \approx 25\%$ in a field of $H = 70$ kOe at a temperature of $T = 31$ K which is close to the ferromagnet–superparamagnet transition temperature. The form of the $\Delta\rho/\rho_0$ dependences is satisfactorily described by the tunneling magnetoresistance mechanism, in which the $\Delta\rho/\rho_0$ value is proportional to the squared magnetization. Thus, the study of a series of Fe–SiO films disclosed the correlation between their transport, magnetotransport, and magnetic properties.

CONFLICT OF INTEREST

The authors declare that they have no conflict of interest.

REFERENCES

1. O. V. Gerashchenko, V. A. Ukleev, E. A. Dyad'kina, A. V. Sitnikov, and Yu. E. Kalinin, Phys. Solid State **59**, 164 (2017).
2. N. V. Volkov, Phys. Usp. **55**, 250 (2012).
3. A. S. Tarasov, M. V. Rautskii, A. V. Lukyanenko, M. N. Volochaev, E. V. Eremin, V. V. Korobtsov, V. V. Balashev, V. A. Vikulov, L. A. Solovyov, and N. V. Volkov, J. Alloys Compd. **688**, 1095 (2016).
4. I. Edelman, M. Esters, D. C. Johnson, G. Yurkin, A. Tarasov, M. Rautsky, M. Volochaev, S. Lyashchenko, R. Ivantsov, D. Petrov, and L. A. Solovyov, J. Magn. Magn. Mater. **443**, 107 (2017).
5. A. B. Granovsky, M. Ilyn, A. Zhukov, V. Zhukova, and J. Gonzalez, Phys. Solid State **53**, 320 (2011).
6. O. Kaman, Z. Jirák, J. Hejtmánek, A. Ndayishimiye, M. Prakasam, and G. Goglio, J. Magn. Magn. Mater. **479**, 135 (2019). https://doi.org/10.1016/j.jmmm.2019.01.114J
7. V. V. Rylkov, S. N. Nikolaev, V. A. Demin, A. V. Emelyanov, A. V. Sitnikov, K. E. Nikirui, V. A. Levanov, M. Yu. Presnyakov, A. N. Taldenkov, A. L. Vasiliev, K. Yu. Chernoglazov, A. S. Vedeneev, Yu. E. Kalinin, A. B. Granovskii, V. V. Tugushev, and A. S. Bugaev, J. Exp. Theor. Phys. **126**, 353 (2018).
8. K. A. Shaykhutdinov, D. A. Balaev, S. V. Semenov, S. I. Popkov, A. A. Dubrovskiy, N. V. Sapronova, and N. V. Volkov, J. Phys. D **44**, 255001 (2011).
9. A. B. Granovskii, Yu. E. Kalinin, M. A. Kashirin, D. V. Kolmakov, V. V. Ryl'kov, A. V. Sitnikov, C. A. Vyzulin, E. A. Gan'shina, and A. N. Taldenkov, J. Exp. Theor. Phys. **125**, 310 (2017).
10. K. A. Shaikhutdinov, D. A. Balaev, S. I. Popkov, S. V. Semenov, N. V. Sapronova, and N. V. Volkov, Phys. Solid State **53**, 2455 (2011).
11. S. V. Komogortsev, E. A. Denisova, R. S. Iskhakov, A. D. Balaev, L. A. Chekanova, Yu. E. Kalinin, and A. V. Sitnikov, J. Appl. Phys. **113**, 17C105 (2013).
12. L. V. Lutsev, Yu. E. Kalinin, A. V. Sitnikov, and O. V. Stognei, Phys. Solid State **44**, 1889 (2002).
13. B. A. Aronzon, D. Yu. Kovalev, A. N. Lagar'kov, E. Z. Meilikhov, V. V. Ryl'kov, M. A. Sedova, N. Negre, M. Goiran, and Dzh. Leotin, JETP Lett. **70**, 90 (1999).
14. K. A. Shaykhutdinov, S. V. Semenov, D. A. Balaev, M. I. Petrov, and N. V. Volkov, Phys. Solid State **51**, 778 (2009).
15. V. V. Rylkov, B. A. Aronzon, A. B. Davydov, D. Yu. Kovalev, and E. Z. Meilikhov, J. Exp. Theor. Phys. **94**, 779 (2002).
16. K. A. Shaykhutdinov, S. I. Popkov, S. V. Semenov, D. A. Balaev, A. A. Dubrovskiy, K. A. Sablina, N. V. Sapronova, and N. V. Volkov, J. Appl. Phys. **109**, 053711 (2011).
17. D. Tripathy, A. O. Adeyeye, and S. Shannigrahi, Phys. Rev. B **76**, 174429 (2007).
18. B. J. Hattink, M. G. del Muro, Z. Konstantinović, X. Batlle, A. Labarta, and M. Varela, Phys. Rev. B **73**, 045418 (2006).
19. B. A. Aronzon, A. E. Varfolomeev, D. Yu. Kovalev, A. A. Likal'ter, V. V. Pyl'kov, and M. A. Sedova, Phys. Solid State **41**, 857 (1999).
20. E. Z. Meilikhov, J. Exp. Theor. Phys. **88**, 819 (1999).
21. E. Z. Meilikhov, JETP Lett. **69**, 623 (1999).
22. E. Z. Meilikhov, B. Raquet, and H. Rakoto, J. Exp. Theor. Phys. **92**, 816 (2001).
23. S. Sankar, A. E. Berkowitz, and D. J. Smith, Phys. Rev. B **62**, 14273 (2000).
24. T. Zhu and Y. J. Wang, Phys. Rev. B **60**, 11918 (1999).
25. S. Honda, T. Okada, M. Nawate, and M. Tokumoto, Phys. Rev. B **56**, 14566 (1997).
26. J. I. Gitelman, Y. Goldstein, and S. Bozovski, Phys. Rev. B **5**, 3609 (1972).
27. S. Barzilai, Y. Goldstein, J. Balberg, and I. S. Helman, Phys. Rev. B **23**, 1809 (1981).
28. B. Abeles, P. Sheng, M. D. Couts, and Y. Arie, Adv. Phys. **24**, 407 (1975).
29. J. S. Helman and B. Abeles, Phys. Rev. Lett. **37**, 1429 (1976).
30. B. P. Khrustalev, A. D. Balaev, and V. G. Pozdnyakov, Thin Solid Films **130**, 195 (1985).
31. B. P. Khrustalev, A. D. Balaev, V. G. Pozdnyakov, and L. I. Vershinina, Sov. Phys. Solid State **27**, 1941 (1985).

32. B. P. Khrustalev, A. D. Balaev, and V. M. Sosnin, Phys. Solid State **37**, 911 (1995).
33. G. K. Celler and L. E. Trimble, Appl. Phys. Lett. **53**, 2492 (1988).
34. J. Goodenough, *Magnetism and the Chemical Bond* (Wiley Intersci., New York, 1963; Metallurgiya, Moscow, 1968).
35. S. Thota, J. H. Shim, and M. S. Seehra, J. Appl. Phys. **114**, 214307 (2013).
36. Yu. A. Kumzerov, N. F. Kartenko, L. S. Parfen'eva, I. A. Smirnov, A. A. Sysoeva, H. Misiorek, and A. Jezowski, Phys. Solid State **54**, 1066 (2012).
37. A. S. Tarasov, A. V. Lukyanenko, I. A. Tarasov, I. A. Bondarev, T. E. Smolyarova, N. N. Kosyrev, V. A. Komarov, I. A. Yakovlev, M. N. Volochaev, L. A. Solovyov, A. A. Shemukhin, S. N. Varnakov, S. G. Ovchinnikov, G. S. Patrin, and N. V. Volkov, Thin Solid Films **642**, 20 (2017).
38. A. S. Tarasov, A. V. Lukyanenko, M. V. Rautskii, I. A. Bondarev, D. A. Smolyakov, I. A. Tarasov, I. A. Yakovlev, S. N. Varnakov, S. G. Ovchinnikov, F. A. Baron, and N. V. Volkov, Semicond. Sci. Technol. **34**, 035024 (2019).
39. Y. Shimada and H. Kojima, J. Appl. Phys. **47**, 4156 (1976).
40. B. P. Khrustalev, A. D. Balaev, and V. M. Sosnin, Solid State Commun. **95**, 271 (1995).
41. A. D. Balaev, Yu. V. Boyarshinov, M. M. Karpenko, and B. P. Khrustalev, Prib. Tekh. Eksp., No. 3, 167 (1985).
42. A. L. Efros and B. I. Shklovskii, J. Phys. C **8**, L49 (1975).
43. D. Gitlin, J. Karp, and B. Moyzhes, J. Phys. D **40**, 2143 (2007).
44. F. Giustino and A. Pasquarello, Microelectron. Eng. **80**, 420 (2005).
45. N. Tomozeiu, Thin Solid Films **516**, 8199 (2008).
46. A. Krywko-Cendrowska, M. Strawski, and M. Szklarczyk, Electrochim. Acta **108**, 112 (2013).
47. N. Tomozeiu, in *Optoelectronics—Materials and Techniques*, Ed. P. Predeep (InTech, Rijeka, 2011).
48. P. M. Tedrov and R. Meservey, Phys. Rev. B **7**, 318 (1973).

Translated by E. Bondareva